Journal of *Marine Science and Engineering*

MDPI

Article

Continuous Characterization of Water-Column Velocity in Cold Seep Plumes Using Pre-Stack Allied Elastic Impedance Inversion

Canping Li [1], Miantao Ma [1], Rui Wang [1], Hairong Zhang [1,*], Yilin Liu [1], Liang Chang [2], Jinqiang Liang [3], Fengying Chen [1] and Binghuang Bao [1]

[1] School of Electronics and Information Engineering, Guangdong Ocean University, Zhanjiang 524088, China; mamiantao@stu.gdou.edu.cn (M.M.)
[2] Research Institute of Geophysical Exploration, Jilin Oilfield Company, PetroChina, Songyuan 138000, China
[3] National Engineering Research Center for Gas Hydrate Exploration and Development, Guangzhou 511458, China
* Correspondence: zhanghr1985@gdou.edu.cn

Abstract

Bubbles in submarine cold-seep plumes cause strong scattering, attenuation, and poor continuity in water-column seismic responses, hindering continuous two-dimensional characterization of acoustic properties. Using multichannel seismic data from the Shenhu area, northern South China Sea, this study proposes a conductivity–temperature–depth (CTD)-constrained, layer-wise two-angle allied elastic impedance (AEI) inversion method to reconstruct water-column velocity. Based on the scattering-equivalent AEI theory, a two-angle equation is derived for layer-wise estimation of water-column velocity, thereby providing a theoretical basis for the subsequent inversion. A relative-amplitude-preserving workflow mitigates bubble-induced attenuation and random scattering, while pre-stack time migration produces common reflection point (CRP) angle gathers. Coherent scattered energy after imaging is parameterized by the local scattering half-angle. Small-angle and large-angle gathers are selected according to effective angular coverage for AEI inversion. CTD-derived seawater velocity and density provide AEI constraints, and the normalized two-angle AEI equation yields a continuous velocity section. Results show velocities of 1460–1560 m/s, with pronounced vertical stratification, relatively weak lateral variation, and agreement between inverted and CTD-derived velocity trends. Within the 0–1800 ms water-column time window, the root-mean-square difference between the inverted and CTD-derived velocities is 18.19 m/s. Combining the lateral continuity of multichannel seismic data with high-accuracy CTD-derived physical-property constraints enables continuous two-dimensional velocity reconstruction in bubble-scattering water columns and offers a new approach for observing cold-seep velocity structure and geophysically characterizing bubble-plume activity.

Keywords: cold seep plume; water-column velocity; allied elastic impedance (AEI); pre-stack inversion; bubble scattering

Check for updates

Academic Editor: Gemma Aiello

Received: 4 August 2026
Revised: 2 September 2026
Accepted: 3 September 2026
Published: 12 September 2026

Copyright: © 2026 by the authors. Licensee MDPI, Basel, Switzerland. This article is an open access article distributed under the terms and conditions of the Creative Commons Attribution (CC BY) license.

1. Introduction

Gas hydrates are regarded as low-carbon, clean energy resources with substantial development potential [1–4], and their occurrence is commonly associated with cold seep activity [5,6]. Submarine cold seep systems are major pathways for the release of deep hydrocarbon fluids, primarily methane. When high-pressure methane escapes from the seafloor into the water column, it forms an ascending structure composed of numerous

bubbles, referred to here as a cold seep plume [7–9]. Previous studies have shown that this gas-release process is closely related to hydrate dissociation, deep-fluid migration, and shallow seepage [5,7,10–12]. Plumes therefore provide direct evidence of seabed gas seepage and also serve as indirect indicators for gas hydrate exploration and identification [8,9,13,14]. Plume bubbles are strongly heterogeneous in space; their presence alters water-column velocity and density and causes complex responses, including acoustic scattering, resonance, and propagation attenuation [15–18]. Compared with identifying only the external geometry of a plume, continuously estimating the acoustic properties within the plume is more useful for analyzing the spatial coupling between bubble perturbations and the background temperature–salinity structure. Water-column velocity is an important physical parameter reflecting the combined effects of the temperature–salinity background and bubble perturbations and is also a key parameter linking multichannel reflection seismic observations to quantitative characterization of cold seep water columns. Stable extraction of a continuous velocity field from complex scattering seismic responses is therefore an important problem in studies of cold seep water-column acoustic structure and seabed fluid activity and provides fundamental physical properties for subsequent gas-content estimation [13,19].

Obtaining a continuous, high-resolution velocity field in a plume-bearing water column has long been challenging. Conventional physical oceanography and underwater acoustics rely mainly on conductivity–temperature–depth (CTD) profilers and single-beam or multibeam sonar. CTD measurements provide seawater temperature, salinity, and pressure, from which high-accuracy velocity and density profiles can be calculated using equations of state for seawater [20–22]. However, bubble distributions within cold seep plumes are strongly heterogeneous and vary dynamically with time. CTD surveys are essentially spatially discrete, single-station vertical observations and cannot capture the complete, continuously evolving two-dimensional structure of a plume [23,24]. High-frequency multibeam and side-scan sonar can delineate the external geometry of a plume at high resolution, but their images primarily reflect the scattering of high-frequency acoustic waves by bubbles. Strong attenuation of acoustic waves in bubble-rich media prevents reconstruction of a macroscale absolute velocity field in the deeper water column along the survey line [8,16,25–28]. The development of seismic oceanography provides a new perspective on this spatial limitation by using high-resolution multichannel seismic (MCS) data to image water-column structures with dense, laterally continuous sampling [23,24,29–32]. Conventional water-column seismic studies generally use post-stack migrated sections. Stacking discards dynamic pre-stack amplitude-versus-angle (AVA) information, making it difficult to establish a stable relationship between seismic amplitude and water-column physical properties. Consequently, continuous two-dimensional velocity inversion remains difficult in water columns affected by complex bubble scattering [13,23,33–37].

Pre-stack methods preserve the dynamic variation of seismic amplitude with incidence angle and offset. Fully exploiting AVA characteristics in MCS gathers therefore provides an important basis for quantitative inversion of seawater physical properties [33–36]. Although acoustic-impedance contrasts across water-column interfaces are small and the associated reflections are weak, pre-stack amplitudes retain a clear angular dependence, making inversion of acoustic properties from multi-angle amplitude responses possible. To overcome the limited spatial continuity of point measurements, wave theory and pre-stack inversion have been introduced into water-column physical-property characterization. Related studies have rederived reflection-coefficient and impedance expressions for water-column interfaces and proposed allied elastic impedance (AEI) theory for marine fluid media [33,34,36,38]. AEI uses multi-angle pre-stack amplitude information to characterize changes in medium properties and quantitatively relates reflection angle

and angle-dependent impedance to variations in seawater velocity and density. Existing AEI frameworks, however, are mostly based on the assumption of a layered continuous medium and are mainly used to characterize temperature–salinity variations and water-column stratification under normal oceanographic conditions. Water columns in cold seep areas are more complex: randomly distributed plume bubbles cause strong scattering, frequency-dependent attenuation, and redistribution of wavefield energy, producing seismic responses typical of random heterogeneous media, including strong scattering, poor continuity, and strong attenuation [15–18,26]. It therefore remains uncertain whether coherent scattered components retained after common reflection point (CRP) imaging can be parameterized effectively by a local scattering half-angle, whether the assumptions of weak local perturbation, single scattering, and linearization remain applicable when these components are incorporated into an AEI framework, and whether the resulting velocity estimates are sufficiently stable and have clearly defined applicability limits.

To address these issues, this study develops a CTD-constrained, layer-wise two-angle AEI velocity inversion method for plume-bearing water columns in cold seep areas using MCS and CTD data from the Shenhu area of the northern South China Sea. The principal contribution is the extension of pre-stack AEI inversion to heterogeneous water columns associated with cold seeps and characterized by bubble scattering, amplitude attenuation, and poor continuity. An integrated workflow combining relative-amplitude-preserving processing, scattering-angle parameterization, layer-wise two-angle inversion, and CTD-derived physical-property constraints is established to achieve continuous quantitative characterization of a two-dimensional velocity field in a complex scattering water column. First, starting from the applicability conditions of conventional water-column AEI, an image-domain representation of the scattered wavefield and a CTD-constrained layer-wise two-angle equation for water-column velocity are developed. Water-column interval extraction, noise attenuation, deconvolution, amplitude compensation, and offset vector tile (OVT)-domain pre-stack time migration are then used to obtain CRP angle gathers that preserve relative amplitudes as closely as possible. Second, the angular response of the coherent scattered component after imaging is represented by the local scattering half-angle, and small-angle and large-angle data are selected by layer according to how their effective coverage varies with two-way time. Third, CTD-derived velocity and density are used to construct low-frequency AEI constraints, and the normalized two-angle AEI relationship is used to recover a continuous two-dimensional velocity field. Finally, the inverted velocity is compared with the CTD-derived velocity, and the effects of bubble scattering and CTD constraints, together with the applicability and uncertainty of the method, are discussed. Section 2 presents the theoretical relationship between the scattered wavefield of a plume and AEI inversion and gives the normalized two-angle AEI equation for velocity recovery; the complete mathematical derivation is provided in Appendix A. Section 3 introduces the study area, MCS and CTD data, and the data-processing workflow. Section 4 describes the scattering-angle-domain transformation and angular-coverage analysis, the construction of CTD-derived AEI constraints and low-frequency models, the layer-wise two-angle AEI inversion, the estimation of data-equivalent exponents, and the recovery of the two-dimensional velocity field in the plume-bearing water column. Section 5 discusses the comparison between inverted and CTD-derived velocities, the roles of bubble scattering and the CTD low-frequency constraint, and the applicability conditions and principal uncertainties. Section 6 summarizes the conclusions and application prospects.

2. Theoretical Background

Conventional reflection-based allied elastic impedance (AEI) and the scattering-equivalent AEI used in this study both exploit the different angular weighting of velocity

and density terms, but they differ in their underlying wavefields and observation relationships. Conventional AEI is defined directly from the specular reflection coefficient of a continuous interface. The measured response of a cold seep plume is instead a superposition of waves scattered within a perturbed region; only the coherent component that retains angular continuity after relative-amplitude-preserving processing and common reflection point (CRP) imaging can be parameterized as an equivalent AEI at the imaging scale. Starting from the applicability conditions of conventional water-column AEI, this section establishes an image-domain representation of the scattered wavefield and presents a CTD-constrained layer-wise two-angle equation for water-column velocity. The complete mathematical derivation is provided in Appendix A.

The seismic response of seawater is governed primarily by variations in P-wave velocity and density. When property contrasts across an interface are small, the acoustic Zoeppritz equation can be linearized [33,38]. The linearized relationship shows that the density-term weight is independent of angle, whereas the velocity-term weight increases with incidence angle. According to the definition of elastic impedance [33,34], the conventional reflection-AEI relationship can be applied directly to reflection data because the effective amplitude is controlled by the interface reflection coefficient, while the incidence angle can be determined from a stable interface normal and the reflected raypath. In a cold seep plume, however, the original amplitude is jointly controlled by volume scattering, propagation attenuation, and illumination; it neither corresponds to a single interface reflection coefficient nor has a stable interface normal. The conventional reflection-AEI relationship therefore cannot be applied directly.

Individual bubbles cannot be resolved by seismic data. The weak perturbation considered here therefore refers to an effective perturbation at the seismic-wavelength and CRP-grid scales. Under conditions of weak perturbations at the imaging scale and when single scattering constitutes the dominant usable energy, the frequency-domain scattered wavefield can be described within a linearized scattering framework [39–42]. OVT-domain pre-stack time migration focuses coherent energy satisfying the propagation-traveltime condition at the CRP location and forms an image-domain scattering response with traceable angular continuity [37,43,44]. Let γ denote the opening angle between the incident and outgoing rays at an image point, and let the local scattering half-angle be θ_s:

$$\theta_s = \frac{\gamma}{2} \tag{1}$$

The opening angle γ is determined by the acquisition geometry, the background migration velocity, and the imaging raypaths. For specular reflection, θ_s is identical to the conventional incidence angle; for plume scattering, θ_s represents the local half-opening angle and does not depend on a stable interface normal. Equation (1) corresponds to the angle transformation and partial-angle stacking of the CRP angle gathers [37,43,44].

Under conditions of weak local effective perturbations and single coherent scattering, and within the high-frequency local plane-wave approximation, the coherent scattering-angle response and the effective property perturbations have an angular-weighting structure analogous to that of fluid reflection, but the two wavefield mechanisms are not identical. Reflection AEI describes velocity and density changes across an interface and uses the interface incidence angle, whereas scattering-equivalent AEI describes velocity and density perturbations relative to the background model and uses the local scattering half-angle in the CRP gather. The normalized scattering-equivalent AEI is

$$\mathrm{AEI}_s^{\mathrm{eq}}(\theta_s) = v_r \rho_e \left(\frac{v_e}{v_r} \right)^{m_s(\theta_s)} \tag{2}$$

where v_e and ρ_e are the effective velocity and density, respectively, of the plume-bearing region at the imaging scale, v_r is the reference velocity, and $m_s(\theta_s)$ is the angular-weighting term corresponding to the local scattering half-angle.

Equation (2) remains a physical-property parameterization. For the kth interval and the jth scattering half-angle range, the three inputs to model-based inversion correspond to the equation variables as follows: the angle-stacked data constrain the finite-band variations in AEI; the angle-dependent wavelet represents the principal bandwidth and phase effects; and the low-frequency model is constructed from the CTD-derived velocity and density. The inversion unknown is the full-band AEI, rather than velocity and density being estimated separately and directly from the seismic data. After obtaining the inverted AEI trace, the data-equivalent exponent is estimated from the trace and CTD-derived physical properties:

$$m_{j,k}^{\mathrm{eq}}(t) = \frac{\ln \mathrm{AEI}_{s,j,k}^{\mathrm{inv}}(t) - \ln[v_r \rho_{\mathrm{CTD}}(t)]}{\ln[v_{\mathrm{CTD}}(t)/v_r]} \tag{3}$$

The inputs to Equation (3) are, in sequence, the inverted AEI trace $\mathrm{AEI}_{s,j,k}^{\mathrm{inv}}(t)$ for the selected angle range, the CTD-derived velocity $v_{\mathrm{CTD}}(t)$, the CTD-derived density $\rho_{\mathrm{CTD}}(t)$, and the reference velocity v_r. Samples for which the denominator approaches zero are excluded, and the robust mean of the valid samples within each interval is adopted as the final $m_{j,k}^{\mathrm{eq}}$.

In this study, CTD data are used to construct the low-frequency model, determine v_r, and estimate the data-equivalent exponent $m_{j,k}^{\mathrm{eq}}$ in Equation (3). The comparison between the inverted velocity and the CTD-derived velocity is therefore an assessment of consistency rather than a fully independent validation. For the kth interval, small-angle and large-angle AEI values are obtained at the same image location. The two AEI datasets must correspond to the same image location and use consistent relative-amplitude scaling, normalization, and low-frequency background scales. Taking logarithms of the two AEI relationships and subtracting them eliminates the common density term, which yields

$$v_e = v_r \exp\left[\frac{\ln \mathrm{AEI}_{s,2,k}^{\mathrm{inv}} - \ln \mathrm{AEI}_{s,1,k}^{\mathrm{inv}}}{m_{2,k}^{\mathrm{eq}} - m_{1,k}^{\mathrm{eq}}}\right] \tag{4}$$

All numerical inputs to Equation (4) are the small-angle and large-angle AEI inversion results $\mathrm{AEI}_{s,1,k}^{\mathrm{inv}}$ and $\mathrm{AEI}_{s,2,k}^{\mathrm{inv}}$, the corresponding data-equivalent exponents $m_{1,k}^{\mathrm{eq}}$ and $m_{2,k}^{\mathrm{eq}}$, and the reference velocity v_r. Density ρ_e is no longer an explicit input; however, angle-dependent amplitude-scaling errors are not eliminated together with the density term. The two angle ranges selected for each interval must both have effective coverage and traceable angular continuity and must retain a sufficiently large exponent difference. Layer-wise angle selection therefore balances common coverage against velocity sensitivity. The specific time intervals and angle ranges are determined from the CRP angle-gather coverage statistics in Section 4.1.

3. Study Area and Data

This section introduces the study area, the original datasets, and the seismic-processing workflow. Marine streamer MCS data are used, with processing designed to preserve weak reflections, weak scattering, and local amplitude variations within the water column above the seafloor, thereby providing a basis for CRP-gather generation, angle-gather extraction, and AEI inversion.

3.1. Study Area and Original Data

The study area is located in the Shenhu area on the northern continental slope of the South China Sea, between the Xisha Trough and the Dongsha Islands, and is an

important region for gas hydrate exploration and cold seep research [45]. Tectonic evolution of the northern South China Sea margin and deep-water sedimentation have produced thick marine sedimentary successions, abundant faults and folds, shallow gas, and fluid-migration-related anomalies, providing favorable conditions for gas hydrate accumulation and the upward migration of deep hydrocarbon-bearing fluids [12,46]. Methane entering the water column through faults, gas chimneys, or highly permeable pathways can form bubble plumes. Previous acoustic studies have identified bubble-plume anomalies on the northern continental slope of the South China Sea [8,47,48], indicating that the region is suitable for water-column velocity inversion using MCS data.

Figure 1 shows a representative raw shot gather from the study area. The seafloor reflection is distinct, and subseafloor reflections are continuous and energetic. In contrast, responses in the water column above the seafloor are weak and mainly appear as local weak events and discontinuous scattering disturbances. The shot gather also contains typical acquisition interference, including ringing, spikes, swell noise, and bird noise. The ringing, spikes, bird noise, and swell noise marked in the figure identify the specific types of interference targeted in the subsequent suppression. Accordingly, a relative-amplitude-preserving workflow is applied to attenuate strong acquisition-related interference while preserving, as much as possible, weak water-column reflections, local scattering, and the relative-amplitude relationships among different offsets.

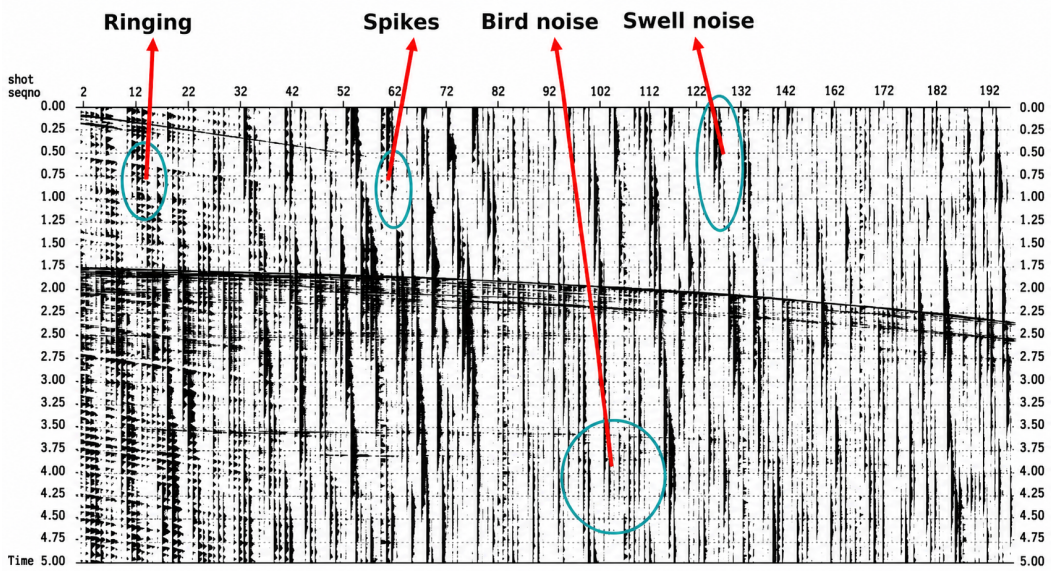
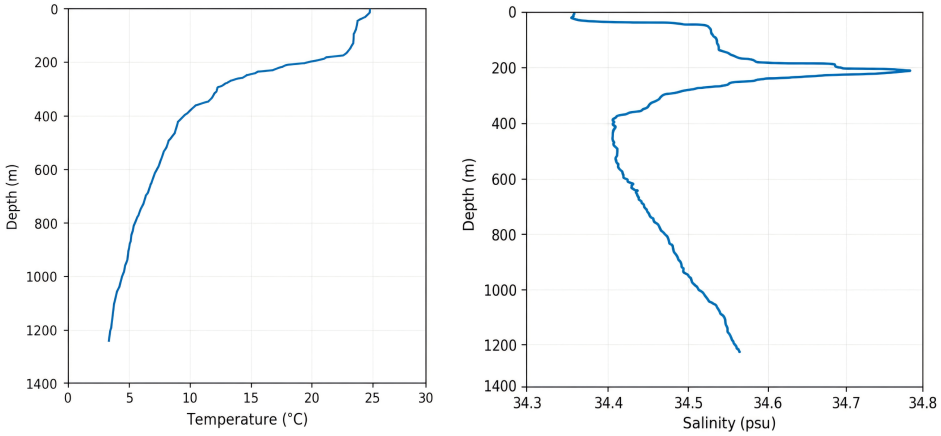


Figure 1. Representative raw shot gather and acquisition-related interference.

In addition to the MCS data, CTD data from the study area are used. The dataset contains water-column temperature, salinity, and depth, and the corresponding temperature and salinity profiles are shown in Figure 2. Temperature generally decreases with depth, changes rapidly in the upper water column, and varies more gradually below approximately 400 m. Salinity fluctuates markedly in the shallow water column, with relatively large variations between approximately 200 and 400 m, and then increases slowly with depth below 400 m. Both temperature and salinity exhibit pronounced vertical variations at depths of approximately 200–400 m, indicating a distinct thermohaline transition within this water layer. Velocity and density profiles calculated from temperature, salinity, and depth are subsequently used to construct AEI constraints and recover water-column velocity in the plume-bearing water column.



(**a**) (**b**)

Figure 2. Variations in CTD temperature and salinity with depth: (**a**) temperature; (**b**) salinity.

3.2. Seismic Data Processing for the Water Column

Cold seep plumes occur primarily in the water column above the seafloor, and their seismic responses are generally characterized by low amplitudes, poor continuity, and local scattering disturbances [13,49]. Because subsequent AEI inversion relies on pre-stack angle-domain amplitudes, processing must suppress acquisition interference while preserving weak water-column responses and relative amplitudes among offsets. The water-column interval is first extracted using the seafloor reflection to reduce interference from reflections of the underlying strata. Subsequently, swell noise, spikes, ringing, bird noise, and horizontal coherent interference are attenuated according to their differences in frequency, amplitude, and coherence characteristics. In the specific processing procedure, spectral analysis is first used to determine the frequency range of low-frequency interference, and a high-pass filter is applied to suppress swell noise. Horizontal coherent interference is then removed in the shot domain, while low-frequency interference such as ringing and bird noise is attenuated. Finally, Yu's wavelet deconvolution is applied to improve resolution [50]. After processing, strong low-frequency interference, local anomalous amplitudes, and acquisition-related noise are substantially reduced, whereas weak events and discontinuous scattering disturbances within the water column are retained.

Following noise attenuation, spherical divergence compensation and surface-consistent amplitude compensation are applied to compensate for energy variations caused by propagation attenuation and differences in acquisition conditions and to improve the amplitude stability of weak water-column responses among offsets. Velocity analysis is then performed using velocity-spectrum picking and multiple iterations. The velocity-picking range in the water column is constrained to 1450–1570 m/s, and far-offset stretch distortion and anomalous traces are muted. After these processing steps, pre-stack time migration is performed in the OVT domain to generate water-column common reflection point (CRP) gathers for subsequent extraction of angle gathers. The processed CRP gather is shown in Figure 3.

As shown in Figure 3, weak events and local scattering disturbances remain identifiable after migration, indicating that plume-related scattering responses are well preserved. The effects of far-offset stretch and anomalous traces are reduced. The processed CRP gathers exhibit improved signal-to-noise ratio and preserve relative amplitudes among different source–receiver combinations, allowing transformation to the local scattering half-angle domain and extraction of angular responses for subsequent AEI inversion.

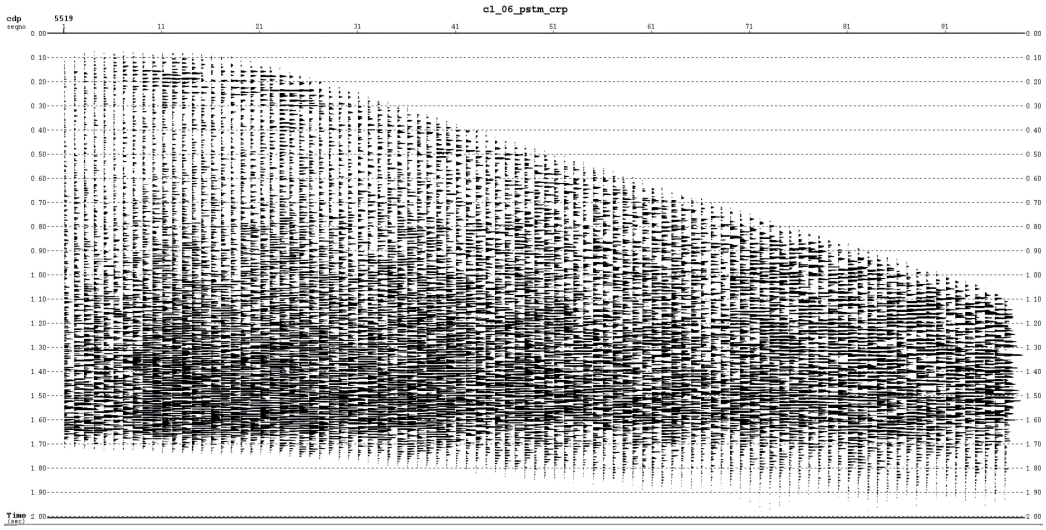


Figure 3. Migrated water-column CRP gather.

To better present the imaging characteristics of the water-column scattering responses, FK-domain filtering was applied before stacking to suppress residual noise, yielding the stacked water-column seismic section shown in Figure 4. As can be seen in the figure, the water-column scattering responses are well imaged, and several localized scattering anomalies exhibit plume-like morphologies, characterized by relatively strong energy in the lower part and progressively weaker energy upward, indicating the presence of plume anomalies in the study area.

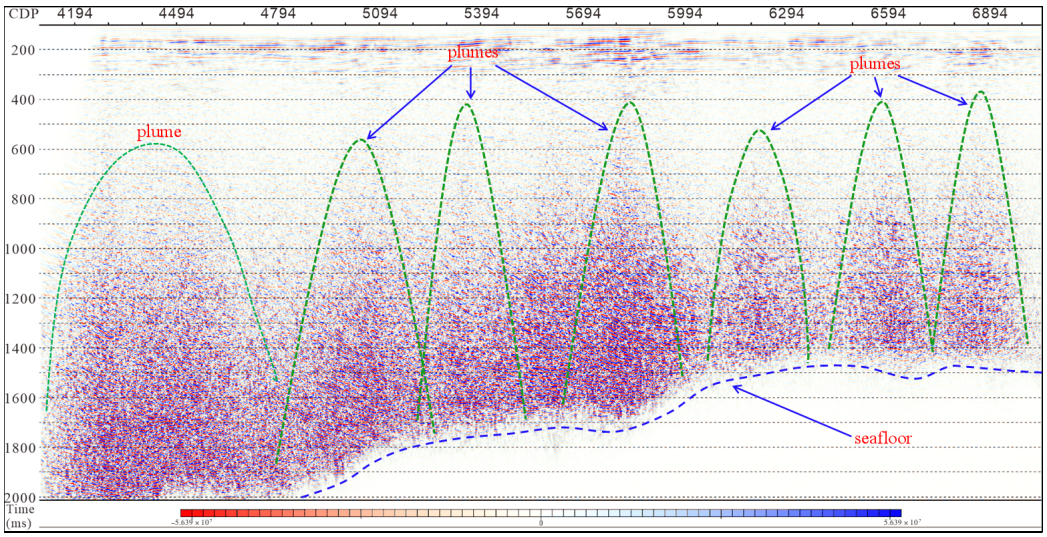


Figure 4. Final stacked seismic section of the cold seep plume. The green dashed curves indicate the interpreted locations of plume anomalies, while the blue dashed line marks the seafloor.

4. Inversion Method and Results

The water-column CRP gathers obtained in Section 3 preserve relative amplitudes for different source–receiver combinations, but the effective coverage of different angles is inconsistent within the water-column time window. Large-angle data progressively disappear with increasing two-way time, and a fixed pair of angle ranges cannot simultaneously ensure effective coverage and adequate angular separation for all water-column intervals. To address this issue, the processed CRP gathers are first transformed into the local scattering half-angle domain. The water column is then divided into intervals according to the effective angular coverage, and small-angle and large-angle stacked data are selected

separately for each interval. Subsequently, CTD-derived velocity and density are used to construct the corresponding angle-specific AEI constraint curves and low-frequency models, and small-angle and large-angle AEI inversions are performed using the corresponding angle-dependent wavelets. On this basis, the data-equivalent exponent for each angle range is estimated from the AEI inversion results and the CTD-derived physical properties. Finally, the two-angle AEI results, the corresponding data-equivalent exponents, and the reference velocity are substituted into Equation (4) to obtain the two-dimensional water-column velocity section.

4.1. Angular-Coverage Analysis and Layer-Wise Inversion Method

AEI inversion requires seismic inputs from two different angle ranges in the water-column CRP gathers. Following Equation (1), for each migrated CRP image point, the local opening angle γ is determined by the source-side and receiver-side imaging raypaths, and half of this opening angle is taken as the local scattering half-angle θ_s. The processed water-column CRP gathers are then transformed into the scattering-angle domain according to θ_s and stacked in 10° intervals to compare the effective angular coverage within the 0–1800 ms water-column time window. The results are listed in Table 1.

Table 1. Effective time coverage corresponding to different angle stacks.

Stack Angle Range (°)	Effective Time Coverage (ms)
5–15	300–1800
15–25	200–1800
25–35	150–1800
35–45	150–1800
45–55	100–1600
55–65	100–1100
65–75	50–700

Table 1 shows substantial differences in effective coverage among angle ranges. Data between 5° and 45° retain usable information in the deeper water column, whereas coverage above 45° decreases progressively with angle. Usable information in the 65–75° range is concentrated mainly in the shallow water column at two-way times of less than 700 ms. Small-angle data therefore provide better deep coverage, whereas large-angle data are concentrated in the shallow and intermediate parts of the water column. A fixed two-angle combination cannot simultaneously provide complete coverage and sufficient angular separation throughout the full water-column window.

Based on these coverage characteristics, a layer-wise inversion strategy is adopted. The 0–1800 ms water-column window is divided into three intervals: 0–599 ms, 600–1199 ms, and 1200–1800 ms. A small-angle and a large-angle range are selected for each interval so that both ranges cover the target interval while maintaining adequate angular separation. The final angle ranges are listed in Table 2.

Table 2. Angle ranges adopted for different water-column intervals.

Two-Way Time (ms)	Small Angle (°)	Large Angle (°)
0–599	50–60	60–70
600–1199	30–40	40–50
1200–1800	10–20	20–30

The selection and processing of angle gathers are illustrated using the large-angle data for the 0–599 ms interval. The large-angle range is 60–70°. Because full-fold coverage is not achieved over the common depth point (CDP) range 4094–4299, the inversion range is restricted to CDP 4300–7000. The angle gather at CDP 4336 is shown in Figure 5.

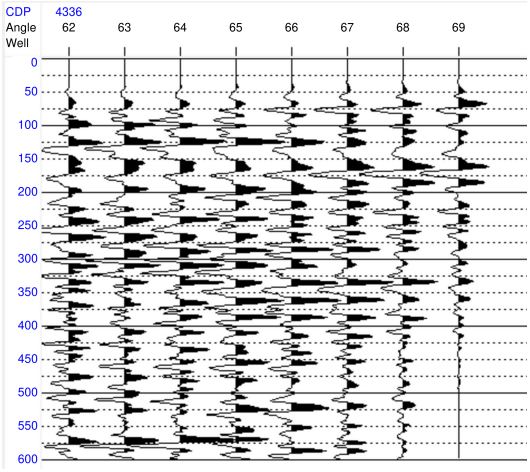


Figure 5. Large-angle gather section (time-axis unit: ms).

As shown in Figure 5, weak scattering events in the upper water column are relatively clear in the migrated CRP gather, and the principal responses show good continuity in the angular direction, indicating that this angle range contains effective information for subsequent AEI inversion. Considering that the effective information in the 65–75° range in Table 1 is concentrated mainly within approximately 50–700 ms, the use of the 60–70° large-angle data for the shallow interval is supported by the actual angular-coverage characteristics of the data. However, because the pseudo-well tie correlation coefficient for this interval is relatively low, the absolute velocity values and local small-scale variations in the shallow water column should be interpreted with greater caution.

The traces within 60–70° are then stacked and the 0–599 ms target window is extracted to obtain the large-angle stacked section for this interval (Figure 6). Angle data for the other intervals are processed in the same manner.

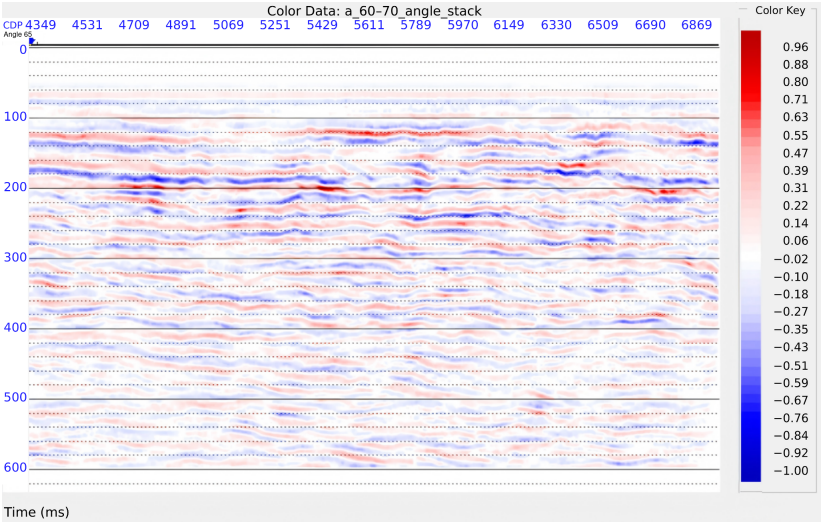
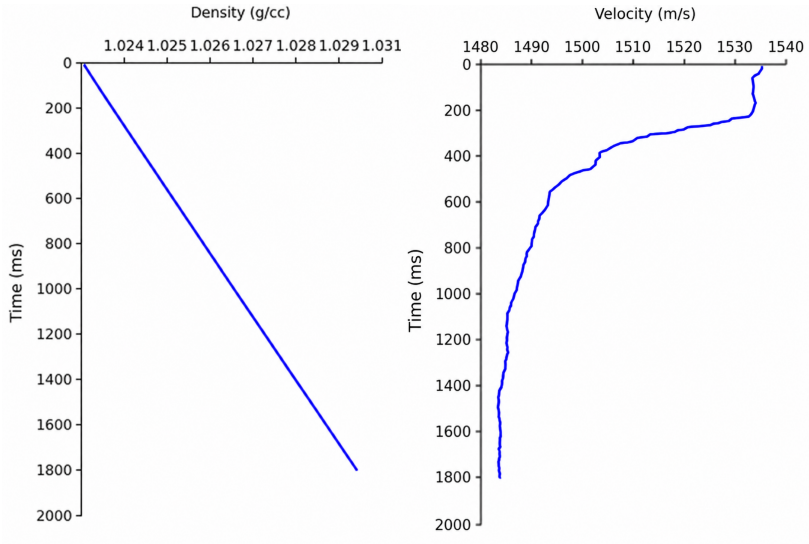


Figure 6. Large-angle stacked section (time-axis unit: ms).

Figure 6 shows that the principal events within the target interval are relatively clear; the stacked data can therefore be used as the seismic input for large-angle AEI inversion in this interval.

4.2. CTD-Derived Physical-Property Profiles and AEI Constraint Construction

Section 4.1 defines the small-angle and large-angle seismic datasets for the different water-column intervals. To establish AEI property constraints at the corresponding angles, water-column velocity and density are calculated from the CTD data. Velocity is computed from temperature, salinity, and depth using the empirical Leroy equation [51], and density is calculated from temperature, salinity, and pressure [22]. The calculated velocity is used to establish a relationship between depth and two-way time, and the velocity and density profiles are transformed into the seismic time domain, as shown in Figure 7.



(**a**) (**b**)

Figure 7. Water-column physical-property profiles calculated from CTD data: (**a**) density; (**b**) velocity.

Figure 7 shows that water density generally increases slowly with two-way time and exhibits a relatively small range of variation. Water-column velocity changes only slightly from 0 to 200 ms, decreases markedly between 200 and 500 ms, and then decreases more gradually after 500 ms, broadly corresponding to the vertical temperature and salinity patterns in Figure 2.

Because different angle ranges are selected for the three intervals, the center of each range in Table 2 is used as its representative angle. The small-angle and large-angle representative values are 55° and 65°, 35° and 45°, and 15° and 25° for the three intervals, respectively. The time-domain velocity and density profiles are substituted into Equation (2), and the mean CTD-derived velocity within the 0–1800 ms water-column time window, 1496.04 m/s, is adopted as the reference velocity v_r to construct the AEI constraint curves for each representative angle, as shown in Figure 8. The same reference velocity is subsequently used in Equations (2)–(4), as well as in Equation (A5) in Appendix A.

The AEI curves at different angles show broadly consistent trends with two-way time, but their numerical differences vary by water-column interval. Angular differences are stronger in the shallow water column and gradually decrease with two-way time. According to the angle combinations in Table 2, the corresponding AEI curves are selected for time calibration and construction of low-frequency models in each interval.

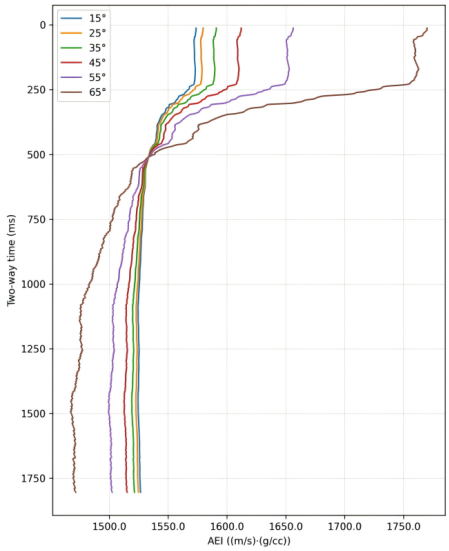
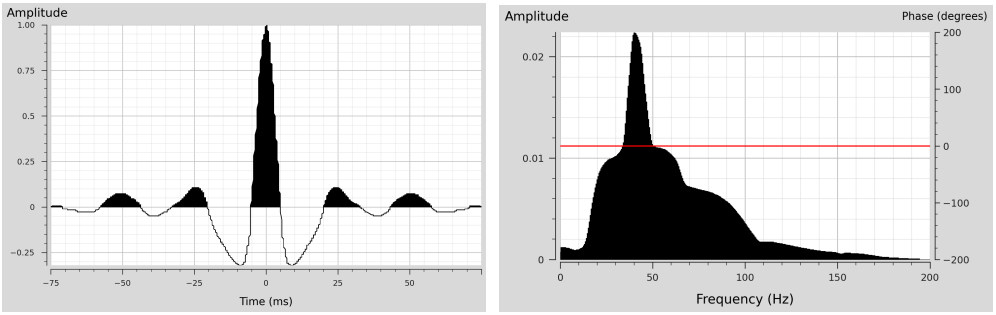


Figure 8. AEI constraint curves at different angles.

4.3. Extraction of Angle-Dependent Wavelets and Construction of Low-Frequency Models

After the AEI constraint curves are obtained, post-stack wavelets are extracted from the angle stacks, followed by a pseudo-well tie. For the 60–70° large-angle data in the 0–599 ms interval, a 150 ms zero-phase post-stack wavelet is estimated statistically. Its time-domain waveform and amplitude spectrum are shown in Figure 9, with most of the spectral energy concentrated between approximately 25 and 65 Hz.



(**a**) (**b**)

Figure 9. Statistically estimated zero-phase post-stack wavelet and its spectrum for the 60–70° large-angle data in the 0–599 ms interval: (**a**) time-domain waveform, with positive-amplitude lobes filled in black; (**b**) amplitude spectrum and phase, with the black fill representing the amplitude spectrum and the red horizontal line indicating a phase of 0°.

The AEI constraint curve at 65° is then treated as a pseudo-well log and convolved with the extracted post-stack wavelet to generate a synthetic seismogram. A pseudo-well tie is performed against the large-angle stacked trace near the CTD location. Spline interpolation is used; the maximum correlation coefficient is first obtained at the default time shift and then optimized by manual fine adjustment. The small-angle data are tied using the corresponding post-stack wavelet and the 55° AEI constraint curve. Maximum cross-correlation coefficients of 0.34 and 0.32 are obtained for the large-angle and small-angle data, respectively. The other intervals are processed in the same manner.

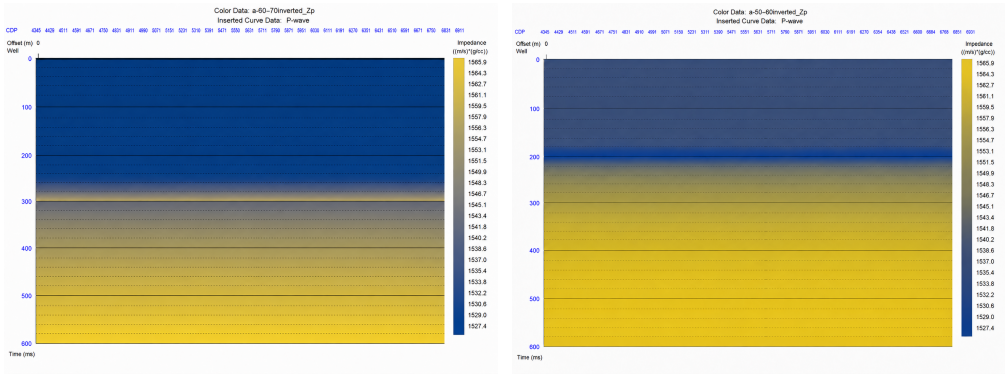
Following the pseudo-well tie, the pre-stack angle-dependent wavelets required for AEI inversion are extracted from the pre-stack data in each angle range. For the large-angle data in the 0–599 ms interval, the 60–70° range is divided into three overlapping sub-angle ranges—60–64°, 63–67°, and 66–70°—and a corresponding pre-stack angle-dependent

wavelet is extracted for each. All extracted wavelets are 150 ms long, have a prominent main lobe, and contain most of their energy between approximately 25 and 80 Hz. The small-angle and large-angle data for the other intervals are processed in the same manner.

Finally, the AEI constraint curves for the representative angles are low-pass filtered according to Equation (A15), retaining frequencies below 10 Hz to construct the corresponding low-frequency AEI models. Seismic data from each sub-angle range, the pre-stack angle-dependent wavelets, and the low-frequency models are used as inputs to model-based inversion. Starting from the low-frequency model, the AEI model is iteratively adjusted until the synthetic records progressively match the observed angle data, yielding small-angle and large-angle AEI inversion results for each water-column interval.

4.4. Allied Elastic Impedance Inversion Constrained by Low-Frequency Models

Following the inversion workflow established in Section 4.3, two-angle AEI inversion is first performed for the 0–599 ms interval. The small-angle and large-angle ranges are 50–60° and 60–70°, respectively, and the inversion extends from CDP 4300 to CDP 7000. The resulting large-angle and small-angle AEI sections are shown in Figure 10.



(**a**) (**b**)

Figure 10. Two-angle AEI inversion results for the 0–599 ms interval: (**a**) large angle; (**b**) small angle.

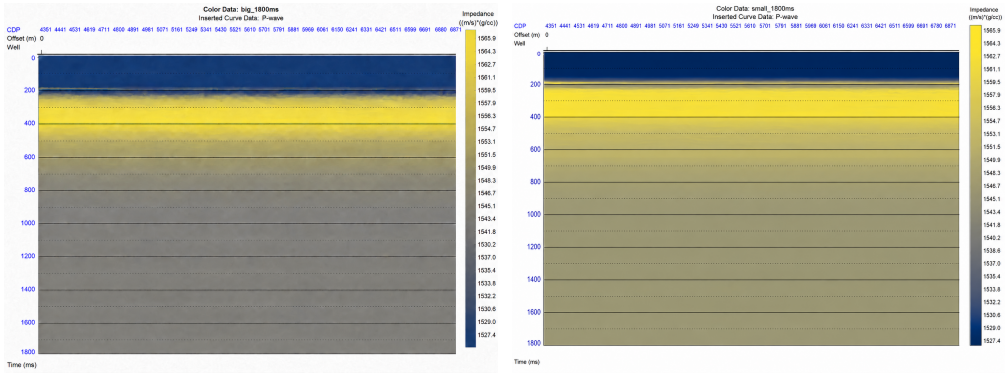
Figure 10 shows that the principal variation intervals differ between the two AEI sections. Large-angle AEI changes most clearly between 260 and 350 ms and then becomes progressively smoother, whereas small-angle AEI varies mainly between 160 and 250 ms and remains relatively stable thereafter.

Using the same workflow, small-angle and large-angle AEI inversions are completed for the 600–1199 ms and 1200–1800 ms intervals. According to the angle combinations in Table 2, the inversion results for the three intervals are merged sequentially over their corresponding two-way time ranges to obtain full-window two-angle AEI sections from 0 to 1800 ms, as shown in Figure 11.

Both the large-angle and small-angle AEI sections in Figure 11 exhibit pronounced vertical stratification and only minor lateral variations within each interval, indicating that water-column properties vary only slightly along the survey line. As two-way time increases, AEI at both angles generally decreases. Values are relatively high in the shallow 0–220 ms interval, corresponding to the marked temperature and salinity variations in that interval. In the middle and deeper parts of the water column, AEI variations gradually diminish; large-angle AEI changes little after 800 ms, whereas small-angle AEI becomes relatively stable after 600 ms.

4.5. Water-Column Velocity Inversion Results for the Plume-Bearing Water Column

Complete small-angle and large-angle AEI sections for the 0–1800 ms water-column window are obtained in Section 4.4. Following the inversion principle in Section 2, small-



(**a**) (**b**)

Figure 11. Full-window two-angle AEI inversion results: (**a**) large angle; (**b**) small angle.

angle and large-angle AEI traces are extracted near the CTD location for each water-column interval. These traces, together with the CTD-derived velocity, density, and reference velocity described in Section 4.2, are substituted into Equation (3). Samples with near-zero denominators are removed, and robust means of valid samples within each interval are used as the data-equivalent exponents for the corresponding angle ranges. The data-equivalent exponents for each interval and their corresponding differences are listed in Appendix Table A1. The two-angle AEI results and corresponding exponents are then substituted into Equation (4), yielding the water-column velocity section of the plume-bearing water column shown in Figure 12.

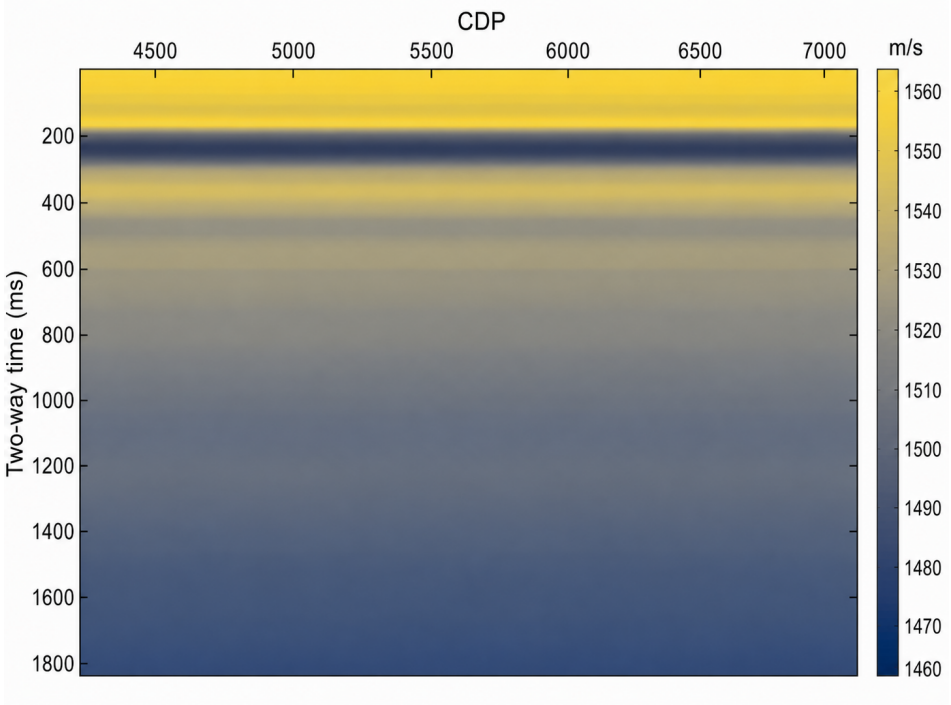


Figure 12. Water-column velocity section of the plume-bearing water column.

As shown in Figure 12, the inverted velocity ranges mainly from 1460 to 1560 m/s. The section exhibits pronounced vertical stratification and only minor lateral variations within each interval, indicating that vertical variations are more pronounced than lateral variations. Velocity is generally higher in the shallow water column and decreases markedly between 200 and 350 ms, broadly corresponding to the thermohaline transition layer. At intermediate and greater depths, velocity variations become progressively more gradual. In

conjunction with the multiple plume anomalies identified in Figure 4, these results indicate that the survey line crosses plume-bearing water columns. The velocity field shown in Figure 12 is dominated by vertical stratification controlled by the thermohaline background, while also containing local velocity perturbations associated with plume bubbles.

5. Discussion

5.1. Comparison Between Inverted Velocities and CTD-Derived Velocities

Section 4.5 presents the water-column velocity section of the plume-bearing water column over the 0–1800 ms time window. Because the inverted velocity varies mainly in the vertical direction and shows relatively minor lateral variations within each interval, the inverted velocity trace at CDP 4399 in Figure 12 is selected for comparison with the CTD-derived velocity profile in Figure 7. The comparison is shown in Figure 13. CDP 4399 is located near the CTD observation station and is therefore used primarily to compare the vertical variation characteristics of the inverted velocity with those of the CTD-derived velocity.

Within 0–150 ms, both curves lie in a relatively high-velocity range and vary only slightly. Between 150 and 400 ms, the inverted velocity decreases rapidly and then rebounds markedly, whereas the CTD-derived velocity generally decreases; their changes are therefore not synchronous. Beyond 400 ms, both curves become progressively smoother, although the inverted velocity is generally higher than the CTD-derived velocity.

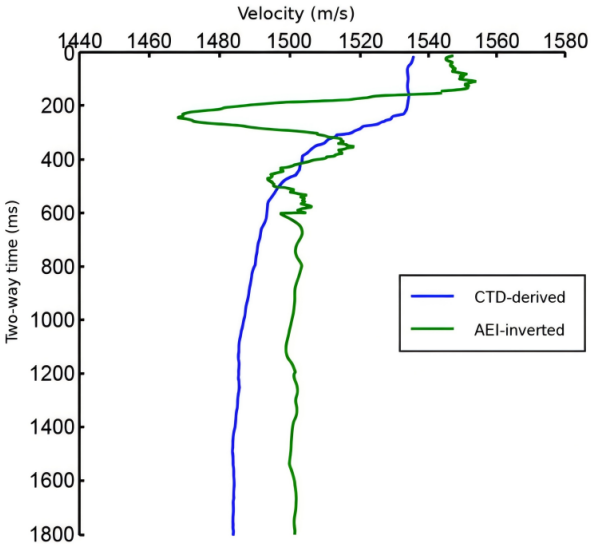


Figure 13. Comparison of the inverted water-column velocity at CDP 4399 with the CTD-derived velocity.

The rapid decrease and subsequent recovery of the inverted velocity between 150 and 400 ms correspond to the thermohaline transition shown in Figure 2 and the main interval of CTD-derived velocity variation in Figure 7. Rapid temperature and salinity changes in this interval may complicate the picking of corresponding energy clusters in the velocity spectrum, and the resulting imaging-velocity uncertainty may indirectly contribute to local fluctuations in the inverted velocity. In addition, the seismic and CTD datasets were acquired at different times, and the water-column temperature–salinity structure may have differed between the two surveys, preventing exact agreement in this interval. Apart from these local discrepancies, the overall trends of the inverted and CTD-derived velocities are similar throughout the 0–1800 ms water-column window.

To further evaluate the consistency between the two velocity estimates, a quantitative comparison was performed within the 0–1800 ms water-column time window. The root-mean-square (RMS) difference is 18.19 m/s, and the Pearson correlation coefficient is 0.489. After excluding the 150–400 ms interval, where relatively large discrepancies occur, the RMS difference decreases to 14.20 m/s and the Pearson correlation coefficient increases to 0.925. These results indicate that the most pronounced discrepancies between the two velocity estimates are concentrated mainly within the 150–400 ms interval, whereas good consistency is observed over the remaining water-column intervals.

In addition, to further assess whether the regional water-column velocity background represented by the CTD-derived velocity in this study is reasonable, publicly available in situ sound-speed profiles from the Shenhu area reported by Wang et al. [52] are introduced for comparison. Over their common depth range of approximately 11–1300 m, the two sound-speed profiles (SVPs) acquired on 4 April and 6 April 2021 yield RMSE values of 5.07 m/s and 3.03 m/s, respectively, relative to the CTD-derived velocity used in this study, with corresponding Pearson correlation coefficients of 0.968 and 0.987. These results indicate that the CTD-derived background velocity adopted in this study is generally consistent with the observed sound-speed structure in the Shenhu area.

It should be noted that the inverted velocity ranges approximately from 1460 to 1560 m/s, whereas the CTD-derived velocity is mainly distributed between approximately 1480 and 1535 m/s. In the inversion, the CTD data primarily provide the low-frequency background and absolute velocity scale, whereas the seismic angle-domain data also contain local water-column variations within the effective seismic bandwidth. Therefore, the velocity ranges obtained from the two datasets are not expected to be completely identical. Local physical-property variations associated with cold seep bubbles may contribute to these differences, while residual noise and processing errors related to amplitude compensation, velocity analysis, migration imaging, angle transformation, and the pseudo-well tie may also produce local velocity fluctuations. Consequently, local variations in the inverted velocity that fall outside the CTD-derived velocity range cannot be attributed solely to bubble effects.

5.2. Influence of Bubble Scattering on AEI Inversion

The plume responses in Figures 3 and 4 mainly appear as short and thin or locally broader scattering disturbances and differ clearly from the long, continuous events associated with water-column interfaces. Previous studies have shown that plume bubbles modify the effective acoustic velocity and density of gas-bearing water and cause scattering, resonance, and propagation attenuation [15–18,26]. Equation (A7) describes bubble-induced local velocity and density perturbations at the imaging scale, and Equations (A11)–(A14) relate these perturbations to the local scattering half-angle and scattering-equivalent AEI. After relative-amplitude-preserving processing and pre-stack time migration, coherent scattered energy is organized by local scattering half-angle, and the influence of plume bubbles is expressed as differences in amplitude and AEI response among angles.

The angular-response relationships in Equations (A11) and (A12) are based on weak local effective perturbations, single coherent scattering, and the high-frequency local plane-wave approximation. The AEI and velocity sections in Figures 11 and 12 exhibit pronounced vertical stratification and only minor lateral variations, indicating that the inversion primarily reflects vertical changes in the temperature–salinity background while also containing local bubble-induced responses. When bubble resonance, multiple scattering, or strong propagation attenuation dominates, the relationship between amplitude variations in CRP angle gathers and first-order velocity and density perturbations weakens, limiting the applicability of scattering-equivalent AEI parameterization. The velocity obtained here

therefore represents the combined effects of the temperature–salinity background and bubble perturbations at the resolution scale of the seismic data and should not be interpreted as the true local acoustic velocity at the scale of individual bubbles or within a localized gas-bearing medium.

5.3. Role of the CTD Low-Frequency Trend Constraint

Figure 7 presents velocity and density profiles calculated from CTD temperature, salinity, and depth, and Figure 8 transforms them into AEI constraint curves at representative angles. Because angle-domain seismic data lack stable low-frequency information, Section 4.3 applies low-pass filtering to the AEI constraint curves to retain components below 10 Hz, thereby constructing small-angle and large-angle low-frequency AEI models for each water-column interval. In contrast to seismic-oceanography studies that primarily use water-column reflections to describe fine thermohaline structure [23,24,29–32], the velocity solution in this study jointly uses a CTD low-frequency background and pre-stack angle-dependent amplitudes. The former supplies the vertical background and absolute scale for AEI inversion, whereas the latter supplies local variations within the effective seismic bandwidth and laterally continuous information along the survey line.

In addition to constructing low-frequency models, CTD data are used to determine the normalized reference velocity and, in Section 4.5, to estimate the data-equivalent exponents for each interval through Equation (3). The comparison in Figure 13 therefore evaluates consistency between the inverted and CTD-derived velocities rather than providing fully independent external validation. Their similar overall trends indicate that the CTD low-frequency constraint effectively constrains the vertical background trend of the velocity field. Local mismatches show that the inversion remains influenced by pre-stack angle-dependent amplitudes and the information contained within the effective seismic bandwidth. Because the current low-frequency model is based on a single CTD profile, its representativeness for the full survey line also affects the results when the thermohaline background varies laterally.

5.4. Applicability Conditions and Uncertainties

Stable application of the method first requires effective two-angle coverage and continuity of angular responses. Because large-angle data occur mainly in the shallow water column, smaller angle combinations must be used at greater depths. The water column should therefore be divided according to actual angular coverage, and both small-angle and large-angle datasets must contain usable information in each interval. Equation (4) indicates that local AEI inversion errors can be amplified during velocity recovery when the difference between the corresponding data-equivalent exponents is small. Each two-angle pair must therefore provide both effective coverage and a sufficiently large exponent difference. The interval division and angle combinations adopted here depend on the acquisition geometry and coverage of the present survey and must be redetermined for other areas. Applicability is reduced when strong attenuation removes effective angular information or multiple scattering destroys angular continuity. The data-equivalent exponents and their differences for the three water-column intervals are listed in Appendix Table A1. The exponent differences for the 0–599 ms, 600–1199 ms, and 1200–1800 ms intervals are 0.03041, 0.15300, and −0.17435, respectively. Among them, the shallow 0–599 ms interval has the smallest absolute exponent difference, indicating that velocity recovery in this interval is relatively more sensitive to local errors in the two-angle AEI inversion.

Although the processing in Section 3 attenuates the principal acquisition interference, residual noise and errors associated with amplitude compensation, velocity analysis, pre-stack time migration, and angle transformation can still affect amplitude relationships

among angle ranges. Angle-dependent wavelet extraction and the pseudo-well tie introduce further uncertainty. Maximum cross-correlation coefficients of 0.34 and 0.32 are obtained for the large-angle and small-angle data in the 0–599 ms interval, respectively, indicating remaining waveform and phase differences between the synthetic and observed data. Because water-column velocity is derived from differences between two-angle AEI values, these errors may affect the corresponding AEI inversion results and subsequently appear as local fluctuations in the recovered velocity.

To further quantify this effect, an amplitude-perturbation test was performed using the retained two-angle AEI data, with detailed results provided in Appendix Table A2. The logarithmic amplitude residuals between the actual AEI values at the calibration location and the CTD-constrained fitted results were used as the perturbation magnitudes. For the small-angle/large-angle data in the three intervals, the RMS relative-amplitude residuals are approximately 0.496%/0.126%, 0.071%/0.087%, and 0.033%/0.064%, respectively. With the CTD background constraint and all other seismic-processing settings held fixed, positive and negative residual perturbations were applied separately to the small-angle and large-angle AEI data. After each perturbation, the calibration procedure was repeated using the same method as in the original inversion, and the velocity solution was recalculated. The four possible positive/negative combinations of the small-angle and large-angle perturbations were tested, and the largest RMS velocity change among them was taken as the sensitivity measure. For the 0–599 ms, 600–1199 ms, and 1200–1800 ms intervals, the maximum RMS velocity changes are 2.06 m/s, 0.92 m/s, and 0.11 m/s, respectively, while the 95th percentiles of the absolute velocity changes are 4.89 m/s, 1.79 m/s, and 0.20 m/s, respectively. Because the data-equivalent exponents were re-estimated using Equation (3) after each perturbation, the reported velocity changes represent the sensitivity of the recalibrated two-angle velocity solution to angle-dependent amplitude perturbations, rather than the results of direct error propagation through Equation (4) with a fixed difference between the data-equivalent exponents.

The results indicate that the shallow-water velocity estimates are relatively more sensitive to angle-dependent amplitude errors, whereas the intermediate-water and deep-water results exhibit better numerical stability. Therefore, the absolute velocity values and local small-scale variations within the 0–599 ms shallow interval should be interpreted more cautiously than those in the intermediate and deeper intervals. The velocity changes described above reflect only the contribution of angle-dependent amplitude perturbations to the uncertainty of the velocity solution under repeated coefficient fitting after each perturbation and should not be regarded as the total uncertainty, which may also include contributions from non-simultaneous observations, residual noise, imaging errors, and other factors.

The velocity-picking range of 1450–1570 m/s used during velocity analysis is employed only to determine an appropriate water-column imaging velocity and to perform pre-stack time migration. It does not define the allowable range of the final velocity solution in Equation (4), and no clipping or restriction of the recovered velocity to 1450–1570 m/s is imposed. The final inverted velocity range of approximately 1460–1560 m/s is determined jointly by the two-angle AEI inversion results, the corresponding data-equivalent exponents, and the reference velocity. Nevertheless, errors in the imaging velocity may affect migration focusing, CRP angle mapping, and relative-amplitude relationships among different angle ranges, and may therefore propagate indirectly into the subsequent AEI inversion and velocity recovery.

During estimation of the data-equivalent exponents, unstable samples for which the denominator in Equation (3) approaches zero are excluded, and robust means of the remaining valid samples within each interval are used to determine the corresponding exponents.

This procedure reduces the influence of locally anomalous samples on exponent estimation. However, the number and proportion of retained or rejected samples may still affect the representativeness of the resulting exponents and should therefore be regarded as an additional source of uncertainty in evaluating the stability of the data-equivalent exponents.

Furthermore, the seismic and CTD datasets were not acquired simultaneously, and the thermohaline structure and plume state may have changed between the two observation periods. The present low-frequency model is constructed from only one CTD profile, and its representativeness along the entire survey line may also affect the inversion results. Between the two observation periods, the positions and magnitudes of the thermocline and halocline may have changed, while the plume and bubble distributions may also have varied with time. These variations may lead to changes in the position of the velocity-transition layer and the magnitude of velocity variations, as well as local differences between the inverted and CTD-derived velocities. Because these water-column variations exhibit pronounced spatial and temporal variability, their effects are unlikely to produce a velocity bias in a fixed direction. Therefore, the discrepancies between the inverted and CTD-derived velocities within the 150–400 ms interval may reflect both real water-column variability and errors associated with data processing and inversion, which cannot be fully separated using the available data.

Future studies could further constrain the lateral variations in the thermohaline background and the spatial distribution of cold seep plumes through simultaneous or near-simultaneous acquisition of MCS, CTD/SVP, and water-column acoustic data, together with increased CTD/SVP sampling along the seismic survey line. Multi-frequency water-column acoustic observations could also provide additional constraints on bubble-scattering responses. On this basis, if parameters such as bubble-size distribution, resonance characteristics, and acoustic attenuation are further obtained, quantitative estimation of bubble volume fraction may become feasible. Estimation of methane flux would additionally require information on gas content, bubble rise velocity, and transport processes.

6. Conclusions

Cold seep plumes provide indirect indicators for gas hydrate exploration and identification. Using MCS and CTD data from the Shenhu area of the northern South China Sea, this study develops a CTD-constrained layer-wise two-angle AEI inversion method and obtains a continuous two-dimensional velocity section of a plume-bearing water column in the cold seep area. The principal findings are as follows:

(1) **Scattering-equivalent AEI and the water-column velocity solution.** To address the scattering, attenuation, and poor continuity of seismic responses caused by plume bubbles, this study distinguishes the wavefield characteristics of continuous-interface reflection from those of bubble-induced volume scattering within the framework of conventional water-column AEI. Coherent scattered components that retain angular continuity after migration of CRP gathers are parameterized using the local scattering half-angle. Under conditions of weak local effective perturbations and single coherent scattering, and within the high-frequency local plane-wave approximation, a relationship is established between velocity and density perturbations and scattering-equivalent AEI. CTD low-frequency models, a reference velocity, and data-equivalent exponents are then introduced, and the common density term is eliminated using the small-angle and large-angle AEI equations, yielding a layer-wise two-angle solution for water-column velocity. This provides the theoretical basis for AEI inversion and continuous velocity characterization in bubble-scattering water columns.

(2) **Seismic data processing for the water column.** To address weak water-column responses, complex acquisition interference, and the susceptibility of pre-stack rel-

ative amplitudes to processing effects, the workflow sequentially applies water-column interval extraction, noise attenuation, deconvolution, amplitude compensation, and velocity analysis, followed by OVT-domain pre-stack time migration to generate water-column CRP gathers. Strong low-frequency interference, local anomalous amplitudes, and acquisition-related noise are substantially reduced, while weak events and local scattering disturbances are retained; far-offset stretch and anomalous-trace effects are also diminished. The resulting CRP gathers preserve relative amplitudes among source–receiver combinations and provide reliable input data for angle-gather extraction and AEI inversion. Multiple water-column scattering responses with plume-like morphologies can be identified in the final stacked section, indicating that the processed seismic data effectively preserve plume-related scattering characteristics.

(3) **Water-column velocity inversion for the plume-bearing water column.** To address inconsistent angular coverage within the water-column window, small-angle and large-angle datasets are selected by layer according to coverage characteristics. CTD-derived velocity and density are used to construct AEI constraints and low-frequency models, and layer-wise two-angle AEI inversion and velocity recovery are completed. Both small-angle and large-angle AEI sections exhibit pronounced vertical stratification and only minor lateral variations. AEI generally decreases with two-way time, with higher values in the shallow water column and progressively smaller variations at intermediate and greater depths. Using the AEI velocity relationship derived here, a continuous two-dimensional velocity section is recovered for the 0–1800 ms water-column window. Inverted velocities range mainly from 1460 to 1560 m/s and are dominated by vertical stratification with only minor lateral variations. Velocity is generally higher in the shallow water column and decreases distinctly between 200 and 350 ms, broadly corresponding to the thermohaline transition, before becoming progressively smoother at greater depths.

(4) **Velocity comparison and method applicability.** Comparison between the inverted velocity at CDP 4399 in Figure 13 and the CTD-derived velocity shows that the two exhibit similar overall trends within the 0–1800 ms water-column time window. The RMS difference is 18.19 m/s, with a Pearson correlation coefficient of $r = 0.489$. After excluding the 150–400 ms interval, the RMS difference decreases to 14.20 m/s and the correlation coefficient increases to $r = 0.925$, indicating that the principal discrepancies between the two velocity estimates are concentrated within this interval, whereas good consistency is observed throughout the remaining water column. Local discrepancies occur from 150 to 400 ms, showing that the result is controlled not only by the thermohaline background but also by local water-column variations represented in the pre-stack angle data. Further analysis indicates that the inverted velocity reflects the combined effects of the temperature–salinity background and bubble perturbations. The CTD low-frequency constraint primarily controls the vertical background and absolute scale, whereas the angle data provide local variations within the effective seismic bandwidth and lateral continuity. Application requires effective two-angle coverage, continuous angular responses, and a sufficiently large difference between data-equivalent exponents. The temporal mismatch between the seismic and CTD surveys, the representativeness of a single CTD station, and residual amplitude errors still affect local results, and the present velocity estimates cannot be directly used to calculate bubble volume fraction or methane flux.

In summary, this study explores a CTD-constrained, layer-wise two-angle AEI velocity inversion method for heterogeneous water columns affected by plume bubbles, providing

a foundation for subsequent estimation of plume gas content and investigation of its relationship with gas hydrate occurrence.

Author Contributions: Conceptualization, C.L. and R.W.; methodology, Y.L.; software, L.C. and F.C.; validation, C.L., R.W. and H.Z.; formal analysis, C.L.; investigation, B.B.; resources, C.L.; data curation, J.L.; writing—original draft preparation, M.M.; writing—review and editing, M.M.; visualization, M.M.; supervision, C.L.; project administration, C.L.; funding acquisition, H.Z. All authors have read and agreed to the published version of the manuscript.

Funding: This research is financially supported by Guangdong Basic and Applied Basic Research Foundation, grant number 2023A1515012041, the Zhanjiang Marine Young Talent Innovation Program, grant number 2025R02101, and the supported by program for scientific research start-up funds of Guangdong Ocean University, grant number 06032112311.

Institutional Review Board Statement: Not applicable.

Informed Consent Statement: Not applicable.

Data Availability Statement: The original MCS data, CTD profile, and inverted velocity section used in this study are project-generated data and are currently subject to project confidentiality restrictions. Therefore, they cannot presently be deposited in a public data repository or made openly accessible through a DOI. Once the relevant confidentiality restrictions are lifted and the conditions for public release are met, standardized sharing through a public data repository will be further considered.

Conflicts of Interest: Author Liang Chang was employed by Research Institute of Geophysical Exploration, Jilin Oilfield Company, PetroChina, Songyuan, China. The remaining authors declare that the research was conducted in the absence of any commercial or financial relationships that could be construed as a potential conflict of interest.

Abbreviations

The following abbreviations are used in this manuscript:

AEI	Allied elastic impedance
AVA	Amplitude versus angle
CDP	Common depth point
CRP	Common reflection point
CTD	Conductivity–temperature–depth
LF	Low frequency
LP	Low-pass filtering operator
MCS	Multichannel seismic
OVT	Offset vector tile

Appendix A. Complete Theoretical Derivation of Scattering-Equivalent AEI and the Layer-Wise Two-Angle Velocity Solution

Appendix A.1. Conventional Water-Column AEI Theory and Its Applicability

The seismic response of seawater is governed primarily by variations in P-wave velocity and density. When property contrasts across an interface are small, the acoustic Zoeppritz equation can be linearized as [33,38]:

$$R_r(\theta) \approx \frac{1}{2}\left(\frac{\Delta\rho}{\bar{\rho}} + \frac{1}{\cos^2\theta}\frac{\Delta v}{\bar{v}}\right) \tag{A1}$$

where R_r is the angle-dependent reflection coefficient at the interface; θ is the incidence angle measured from the interface normal; $\bar{v}$ and $\bar{\rho}$ are the mean velocity and density, respectively, on the two sides of the interface; and Δv and $\Delta\rho$ are the corresponding parameter contrasts. Under the weak-contrast approximation,

$$R_r(\theta) \approx \frac{1}{2}[\Delta \ln \rho + m_r(\theta)\Delta \ln v] \tag{A2}$$

$$m_r(\theta) = \sec^2\theta = 1 + \tan^2\theta \tag{A3}$$

Equation (A2) shows that the density-term weight is independent of angle, whereas the velocity-term weight increases with incidence angle. According to the definition of elastic impedance [33,34],

$$R_r(\theta) \approx \frac{1}{2}\Delta \ln \mathrm{AEI}_r(\theta) \tag{A4}$$

Combining Equations (A2) and (A4) and introducing normalization by the reference velocity v_r gives

$$\mathrm{AEI}_r(\theta) = v_r\rho\left(\frac{v}{v_r}\right)^{m_r(\theta)} \tag{A5}$$

Equation (A5) describes the physical relationship among velocity, density, incidence angle, and reflection AEI; AEI is not obtained by directly substituting the three inversion inputs into this equation. For the jth reflection-angle range, the actual observation equation is

$$d_{r,j}^{\mathrm{obs}} = w_{r,j} * \left[\frac{1}{2}\Delta \ln \mathrm{AEI}_{r,j}\right] + n_{r,j} \tag{A6}$$

where $d_{r,j}^{\mathrm{obs}}$ is the angle-stacked seismic data, $w_{r,j}$ is the corresponding angle-dependent wavelet, $n_{r,j}$ is noise, and $\mathrm{AEI}_{r,j}$ is the model to be inverted. The low-frequency model is constructed by substituting the CTD-derived velocity v_{CTD} and density ρ_{CTD} into Equation (A5); v_r is taken as a representative CTD-derived velocity, and $m_{r,j}$ is determined by the reflection incidence angle. Thus, the angle stack constrains variations in $\mathrm{AEI}_{r,j}$ within the seismic frequency band, the wavelet establishes the forward relationship between $\Delta \ln \mathrm{AEI}_{r,j}$ and seismic amplitude, and the CTD low-frequency model provides the long-wavelength background and absolute scale.

Equation (A5) can be applied directly to conventional reflection data because the effective amplitude in Equation (A6) is controlled by the interface reflection coefficient R_r, and Equation (A4) establishes a direct relationship between R_r and $\Delta \ln \mathrm{AEI}_r$. In addition, the incidence angle can be determined from a stable interface normal and the reflected raypath. In a cold seep plume, however, the original amplitude is jointly controlled by volume scattering, propagation attenuation, and illumination; it neither corresponds to a single interface reflection coefficient nor has a stable interface normal. Equation (A5) therefore cannot be applied directly.

Appendix A.2. Image-Domain Representation of the Scattered Wavefield of a Cold Seep Plume

Individual bubbles cannot be resolved by seismic data. The weak perturbation considered here therefore refers to an effective perturbation at the seismic-wavelength and CRP-grid scales. Let the background water-column properties be $v_b(\mathbf{x})$ and $\rho_b(\mathbf{x})$, and let the effective properties of the plume-bearing region be $v_e(\mathbf{x})$ and $\rho_e(\mathbf{x})$; then

$$v_e = v_b + \delta v_e, \qquad \rho_e = \rho_b + \delta\rho_e \tag{A7}$$

Here, δv_e and $\delta\rho_e$ denote local effective perturbations relative to the background model; they differ from the interface contrasts Δv and $\Delta\rho$ in Equations (A1) and (A2). Extraction

of the water-column interval confines the target region of Equation (A7), whereas noise attenuation suppresses observed components unrelated to medium perturbations.

When perturbations are weak at the imaging scale and single scattering constitutes the dominant usable energy, the frequency-domain scattered wavefield can be written as [39–42]

$$U_s(\mathbf{x}_s, \mathbf{x}_r, \omega) = \int_\Omega A(\mathbf{x}_s, \mathbf{x}_r, \mathbf{x}, \omega) S_e(\mathbf{x}, \omega) e^{i\omega\Phi} \, \mathrm{d}\mathbf{x} \tag{A8}$$

Here, $\mathbf{x}_s$, $\mathbf{x}_r$, and $\mathbf{x}$ denote the source, receiver, and scattering-point positions, respectively; S_e is the scattering term generated by δv_e and $\delta\rho_e$; A includes the source wavelet, geometrical spreading, propagation attenuation, and illumination; and Φ is the propagation traveltime. Equation (A8) explains the generation mechanism of the original scattered wavefield and is not a direct input to the subsequent AEI inversion. The acquisition geometry provides $\mathbf{x}_s$ and $\mathbf{x}_r$, whereas the background velocity controls Φ; deconvolution, spherical divergence compensation, and relative-amplitude compensation primarily reduce the non-property-related variations contained in A.

OVT-domain pre-stack time migration uses the background velocity to focus coherent energy satisfying the traveltime condition at the CRP location [37,43,44]. The migrated angle-domain amplitude can be summarized as

$$I_s(\mathbf{x}, \theta_s, \omega) \approx C(\mathbf{x}, \theta_s, \omega) Q_s(\mathbf{x}, \theta_s) + N_s \tag{A9}$$

In Equation (A9), I_s is obtained directly from the migrated CRP angle gather; C represents the residual wavelet, illumination, attenuation, and migration-scaling factors, with its bandwidth and phase described by the angle-dependent wavelet and its angle-dependent scaling controlled as far as possible through relative-amplitude-preserving processing; Q_s is the imaging-scale equivalent scattering-angle response to be recovered; and N_s includes residual noise, multiple scattering, and unmodeled wavefield components. Energy that does not retain angular continuity after migration is assigned to N_s and is excluded from AEI parameterization.

Let γ denote the opening angle between the incident and outgoing rays at an image point, and let the local scattering half-angle be θ_s:

$$\theta_s = \frac{\gamma}{2} \tag{A10}$$

The opening angle γ is determined by the acquisition geometry, the background migration velocity, and the imaging raypaths. For specular reflection, θ_s is identical to the conventional incidence angle; for plume scattering, θ_s represents the local half-opening angle and does not depend on a stable interface normal. Equation (A10) corresponds to the angle transformation and partial-angle stacking of the CRP angle gathers [37,43,44].

Appendix A.3. Scattering-Equivalent AEI and Its Relationship to Reflection AEI

Under conditions of weak local effective perturbations and single coherent scattering, and within the high-frequency local plane-wave approximation, Q_s can be written as follows, provided that C in Equation (A9) has been controlled or is represented by the angle-dependent wavelet:

$$Q_s(\theta_s) \approx \frac{1}{2}[\delta \ln \rho_e + m_s(\theta_s) \delta \ln v_e] \tag{A11}$$

$$m_s(\theta_s) \approx \sec^2 \theta_s \tag{A12}$$

Equation (A11) indicates only that the coherent scattering-angle response and the effective property perturbations have an angular-weighting structure analogous to that of fluid reflection; it does not imply that the two wavefield mechanisms are identical. Reflection AEI describes $\Delta \ln v$ and $\Delta \ln \rho$ across an interface and uses the interface incidence angle, whereas scattering-equivalent AEI describes $\delta \ln v_e$ and $\delta \ln \rho_e$ relative to the background model and uses the local scattering half-angle θ_s in the CRP gather.

Define

$$Q_s(\theta_s) \approx \frac{1}{2}\delta \ln \mathrm{AEI}_s^{\mathrm{eq}}(\theta_s) \tag{A13}$$

The normalized scattering-equivalent AEI is then

$$\mathrm{AEI}_s^{\mathrm{eq}}(\theta_s) = v_r \rho_e \left(\frac{v_e}{v_r}\right)^{m_s(\theta_s)} \tag{A14}$$

Equation (A14) remains a physical-property parameterization. For the kth interval and the jth scattering half-angle range, the three inputs to model-based inversion correspond to the equation variables as follows: the angle-stacked data $d_{s,j,k}^{\mathrm{obs}}$, derived from I_s in Equation (A9), constrain the finite-band variations in $\mathrm{AEI}_{s,j,k}^{\mathrm{eq}}$; the angle-dependent wavelet $w_{s,j,k}$ represents the principal bandwidth and phase effects of C in Equation (A9); and the low-frequency model is constructed from

$$\mathrm{AEI}_{s,j,k}^{\mathrm{LF}} = \mathrm{LP}\left\{ v_r \rho_{\mathrm{CTD}} \left(\frac{v_{\mathrm{CTD}}}{v_r}\right)^{m_{j,k}^{(0)}} \right\} \tag{A15}$$

where $\mathrm{AEI}_{s,j,k}^{\mathrm{LF}}$ denotes the low-frequency (LF) AEI model, $\mathrm{LP}\{\cdot\}$ denotes low-pass filtering, and $m_{j,k}^{(0)} = \sec^2 \theta_{c,j,k}$ is determined by the central angle $\theta_{c,j,k}$ of the selected angle range. The inversion unknown is the full-band $\mathrm{AEI}_{s,j,k}$, rather than v_e and ρ_e being estimated separately and directly from the seismic data. After obtaining the inverted AEI trace, an equivalent exponent is estimated from the trace and CTD-derived physical properties (here termed the data-equivalent exponent):

$$m_{j,k}^{\mathrm{eq}}(t) = \frac{\ln \mathrm{AEI}_{s,j,k}^{\mathrm{inv}}(t) - \ln[v_r \rho_{\mathrm{CTD}}(t)]}{\ln[v_{\mathrm{CTD}}(t)/v_r]} \tag{A16}$$

The inputs to Equation (A16) are, in sequence, the inverted AEI trace $\mathrm{AEI}_{s,j,k}^{\mathrm{inv}}$ for the selected angle range, the CTD-derived velocity v_{CTD}, the CTD-derived density ρ_{CTD}, and the reference velocity v_r. Samples for which the denominator approaches zero are excluded, and the robust mean of the valid samples within each interval is adopted as the final $m_{j,k}^{\mathrm{eq}}$.

Appendix A.4. CTD-Constrained Layer-Wise Two-Angle Velocity Solution

In this study, CTD data are used to construct the low-frequency model in Equation (A15), determine v_r, and estimate the data-equivalent exponent $m_{j,k}^{\mathrm{eq}}$ in Equation (A16). The comparison between the inverted velocity and the CTD-derived velocity is therefore an assessment of consistency rather than a fully independent validation.

For the kth interval, small-angle and large-angle AEI values are obtained at the same image location:

$$\mathrm{AEI}_{s,1,k}^{\mathrm{inv}} = v_r \rho_e \left(\frac{v_e}{v_r}\right)^{m_{1,k}^{\mathrm{eq}}} \tag{A17}$$

$$\mathrm{AEI}_{s,2,k}^{\mathrm{inv}} = v_r \rho_e \left(\frac{v_e}{v_r}\right)^{m_{2,k}^{\mathrm{eq}}} \tag{A18}$$

The direct inputs to Equations (A17) and (A18) are the two model-based inversion outputs $AEI^{inv}_{s,1,k}$ and $AEI^{inv}_{s,2,k}$, together with the corresponding data-equivalent exponents $m^{eq}_{1,k}$ and $m^{eq}_{2,k}$ obtained from Equation (A16). The reference velocity v_r is determined from the CTD data, v_e is the target quantity, and ρ_e is the unknown shared by the two equations. The two AEI datasets must correspond to the same image location and use consistent relative-amplitude scaling, normalization, and low-frequency background scales.

Taking logarithms of the two equations and subtracting them eliminates the common density term:

$$\ln AEI^{inv}_{s,2,k} - \ln AEI^{inv}_{s,1,k} = \left(m^{eq}_{2,k} - m^{eq}_{1,k}\right) \ln\left(\frac{v_e}{v_r}\right) \tag{A19}$$

which yields

$$v_e = v_r \exp\left[\frac{\ln AEI^{inv}_{s,2,k} - \ln AEI^{inv}_{s,1,k}}{m^{eq}_{2,k} - m^{eq}_{1,k}}\right] \tag{A20}$$

All numerical inputs to Equation (A20) are the small-angle and large-angle AEI inversion results $AEI^{inv}_{s,1,k}$ and $AEI^{inv}_{s,2,k}$, the corresponding data-equivalent exponents $m^{eq}_{1,k}$ and $m^{eq}_{2,k}$, and the reference velocity v_r. Density ρ_e is no longer an explicit input; however, angle-dependent amplitude-scaling errors are not eliminated together with the density term. The two angle ranges selected for each interval must both have effective coverage and traceable angular continuity and must retain a sufficiently large exponent difference. Layer-wise angle selection therefore balances common coverage against velocity sensitivity. The specific time intervals and angle ranges are determined from the CRP angle-gather coverage statistics in Section 4.1.

Table A1. Data-equivalent exponents and their differences for the three water-column intervals.

Water-Column Interval	Small-Angle Range	Large-Angle Range	Small-Angle m_{eq}	Large-Angle m_{eq}	Δm_{eq}
0–599 ms	50–60°	60–70°	0.95161	0.98202	0.03041
600–1199 ms	30–40°	40–50°	1.03434	1.18734	0.15300
1200–1800 ms	10–20°	20–30°	0.69799	0.52364	−0.17435

Table A2. Results of the amplitude-perturbation test for the three water-column intervals.

Water-Column Interval	Small-Angle Residual RMS (%)	Large-Angle Residual RMS (%)	Maximum RMS Δv (m/s)	P95 of $\lvert\Delta v\rvert$ (m/s)
0–599 ms	0.496	0.126	2.06	4.89
600–1199 ms	0.071	0.087	0.92	1.79
1200–1800 ms	0.033	0.064	0.11	0.20

References

1. Kvenvolden, K.A. Gas hydrates—Geological perspective and global change. *Rev. Geophys.* **1993**, *31*, 173–187. [CrossRef]
2. Sloan, E.D.; Koh, C.A. *Clathrate Hydrates of Natural Gases*, 3rd ed.; CRC Press: Boca Raton, FL, USA, 2007. [CrossRef]
3. Boswell, R.; Collett, T.S. Current perspectives on gas hydrate resources. *Energy Environ. Sci.* **2011**, *4*, 1206–1215. [CrossRef]
4. Chong, Z.R.; Yang, S.H.B.; Babu, P.; Linga, P.; Li, X.-S. Review of natural gas hydrates as an energy resource: Prospects and challenges. *Appl. Energy* **2016**, *162*, 1633–1652. [CrossRef]
5. Torres, M.E.; Wallmann, K.; Tréhu, A.M.; Bohrmann, G.; Borowski, W.S.; Tomaru, H. Gas hydrate growth, methane transport, and chloride enrichment at the southern summit of Hydrate Ridge, Cascadia margin off Oregon. *Earth Planet. Sci. Lett.* **2004**, *226*, 225–241. [CrossRef]
6. Liang, Q.; Hu, Y.; Feng, D.; Peckmann, J.; Chen, L.; Yang, S.; Liang, J.; Tao, J.; Chen, D. Authigenic carbonates from newly discovered active cold seeps on the northwestern slope of the South China Sea: Constraints on fluid sources, formation environments, and seepage dynamics. *Deep-Sea Res. Part I Oceanogr. Res. Pap.* **2017**, *124*, 31–41. [CrossRef]
7. Mau, S.; Tu, T.-H.; Becker, M.; dos Santos Ferreira, C.; Chen, J.-N.; Lin, L.-H.; Wang, P.-L.; Lin, S.; Bohrmann, G. Methane seeps and independent methane plumes in the South China Sea offshore Taiwan. *Front. Mar. Sci.* **2020**, *7*, 543. [CrossRef]

8. Liu, B.; Liu, S.X. Gas bubble plumes observed at north slope of South China Sea from multi-beam water column data. *Haiyang Xuebao* **2017**, *39*, 83–89. (In Chinese) [CrossRef]
9. Greinert, J.; Artemov, Y.; Egorov, V.; De Batist, M.; McGinnis, D. 1300-m-high rising bubbles from mud volcanoes at 2080 m in the Black Sea: Hydroacoustic characteristics and temporal variability. *Earth Planet. Sci. Lett.* **2006**, *244*, 1–15. [CrossRef]
10. Ruppel, C.D.; Kessler, J.D. The interaction of climate change and methane hydrates. *Rev. Geophys.* **2017**, *55*, 126–168. [CrossRef]
11. Zhang, X.; Du, Z.; Luan, Z.; Wang, X.; Xi, S.; Wang, B.; Li, L.; Lian, C.; Yan, J. In situ Raman detection of gas hydrates exposed on the seafloor of the South China Sea. *Geochem. Geophys. Geosyst.* **2017**, *18*, 3700–3713. [CrossRef]
12. Ren, J.; Cheng, C.; Jiang, T.; Kuang, Z.; Lai, H.; Liang, J.; Chen, Z.; Li, T. Faults and gas chimneys jointly dominate the gas hydrate accumulation in the Shenhu Area, northern South China Sea. *Front. Mar. Sci.* **2023**, *10*, 1254410. [CrossRef]
13. Chen, J.; Tong, S.; Han, T.; Song, H.; Pinheiro, L.M.; Xu, H.; Azevedo, L.; Duan, M.; Liu, B. Modelling and detection of submarine bubble plumes using seismic oceanography. *J. Mar. Syst.* **2020**, *209*, 103375. [CrossRef]
14. Paull, C.K.; Ussler, W., III; Borowski, W.S.; Spiess, F.N. Methane-rich plumes on the Carolina continental rise: Associations with gas hydrates. *Geology* **1995**, *23*, 89–92. [CrossRef]
15. Minnaert, M. On musical air-bubbles and the sounds of running water. *Philos. Mag.* **1933**, *16*, 235–248. [CrossRef]
16. Commander, K.W.; Prosperetti, A. Linear pressure waves in bubbly liquids: Comparison between theory and experiments. *J. Acoust. Soc. Am.* **1989**, *85*, 732–746. [CrossRef]
17. Prosperetti, A. The speed of sound in a gas–vapour bubbly liquid. *Interface Focus* **2015**, *5*, 20150024. [CrossRef] [PubMed]
18. Foldy, L.L. The multiple scattering of waves. I. General theory of isotropic scattering by randomly distributed scatterers. *Phys. Rev.* **1945**, *67*, 107–119. [CrossRef]
19. Han, T.; Chen, J.; Azevedo, L.; He, B.; Xu, H.; Yang, R. Quantitative estimation of bubble volume fraction of submarine seep plumes by modeling seismic oceanography data. *J. Oceanol. Limnol.* **2023**, *41*, 673–686. [CrossRef]
20. Chen, C.-T.; Millero, F.J. Speed of sound in seawater at high pressures. *J. Acoust. Soc. Am.* **1977**, *62*, 1129–1135. [CrossRef]
21. Mackenzie, K.V. Nine-term equation for sound speed in the oceans. *J. Acoust. Soc. Am.* **1981**, *70*, 807–812. [CrossRef]
22. Millero, F.J.; Chen, C.-T.; Bradshaw, A.; Schleicher, K. A new high pressure equation of state for seawater. *Deep-Sea Res. Part A Oceanogr. Res. Pap.* **1980**, *27*, 255–264. [CrossRef]
23. Azevedo, L.; Matias, L.; Turco, F.; Tromm, R.; Peliz, Á. Geostatistical seismic inversion for temperature and salinity in the Madeira Abyssal Plain. *Front. Mar. Sci.* **2021**, *8*, 685007. [CrossRef]
24. Chakraborty, D.; Mallick, S. Estimation of temperature and salinity from marine seismic data—A two-step approach. *J. Mar. Sci. Eng.* **2024**, *12*, 471. [CrossRef]
25. Urban, P.; Veloso-Alarcón, M.E.; Greinert, J. Echo grid integration: A novel method for preprocessing multibeam water column data to quantify underwater gas bubble emissions. *Limnol. Oceanogr. Methods* **2023**, *21*, 377–400. [CrossRef]
26. Veloso, M.; Greinert, J.; Mienert, J.; De Batist, M. A new methodology for quantifying bubble flow rates in deep water using splitbeam echosounders: Examples from the Arctic offshore NW-Svalbard. *Limnol. Oceanogr. Methods* **2015**, *13*, 267–287. [CrossRef]
27. Blomberg, A.E.A.; Sæbø, T.O.; Hansen, R.E.; Pedersen, R.B.; Austeng, A. Automatic detection of marine gas seeps using an interferometric sidescan sonar. *IEEE J. Ocean. Eng.* **2017**, *42*, 590–602. [CrossRef]
28. Pan, H.; Tang, K.; Zhuo, J.; Lu, Y.; Chen, J.; Lv, Z. Underwater acoustic technology-based monitoring of oil spill: A review. *J. Mar. Sci. Eng.* **2023**, *11*, 870. [CrossRef]
29. Holbrook, W.S.; Páramo, P.; Pearse, S.; Schmitt, R.W. Thermohaline fine structure in an oceanographic front from seismic reflection profiling. *Science* **2003**, *301*, 821–824. [CrossRef] [PubMed]
30. Ruddick, B.; Song, H.; Dong, C.; Pinheiro, L. Water column seismic images as maps of temperature gradient. *Oceanography* **2009**, *22*, 192–205. [CrossRef]
31. Sallarès, V.; Biescas, B.; Buffett, G.; Carbonell, R.; Dañobeitia, J.J.; Pelegrí, J.L. Relative contribution of temperature and salinity to ocean acoustic reflectivity. *Geophys. Res. Lett.* **2009**, *36*, L00D06. [CrossRef]
32. Dickinson, A.; Gunn, K.L. The next decade of seismic oceanography: Possibilities, challenges and solutions. *Front. Mar. Sci.* **2022**, *9*, 736693. [CrossRef]
33. Connolly, P. Elastic impedance. *Lead. Edge* **1999**, *18*, 438–452. [CrossRef]
34. Whitcombe, D.N. Elastic impedance normalization. *Geophysics* **2002**, *67*, 60–62. [CrossRef]
35. Lu, S.; McMechan, G.A. Elastic impedance inversion of multichannel seismic data from unconsolidated sediments containing gas hydrate and free gas. *Geophysics* **2004**, *69*, 164–179. [CrossRef]
36. Liu, X.; Liu, H.; Zhu, J.; Wei, J. Inversion of seawater physical properties based on allied elastic impedance. *J. Water Resour. Prot.* **2016**, *8*, 135–142. [CrossRef]
37. Brandsberg-Dahl, S.; de Hoop, M.V.; Ursin, B. Focusing in dip and AVA compensation on scattering-angle/azimuth common image gathers. *Geophysics* **2003**, *68*, 232–254. [CrossRef]
38. Zhu, J.Q. Application of Allied Elastic Impedance Inversion in the Study of Ocean Characteristics. Master's Thesis, Ocean University of China, Qingdao, China, 2014. (In Chinese)

39. Wu, R.-S.; Aki, K. Scattering characteristics of elastic waves by an elastic heterogeneity. *Geophysics* **1985**, *50*, 582–595. [CrossRef]
40. Beylkin, G.; Burridge, R. Linearized inverse scattering problems in acoustics and elasticity. *Wave Motion* **1990**, *12*, 15–52. [CrossRef]
41. Shaw, R.K.; Sen, M.K. Born integral, stationary phase and linearized reflection coefficients in weak anisotropic media. *Geophys. J. Int.* **2004**, *158*, 225–238. [CrossRef]
42. Aki, K.; Richards, P.G. *Quantitative Seismology: Theory and Methods*; W.H. Freeman: San Francisco, CA, USA, 1980.
43. Xu, S.; Chauris, H.; Lambaré, G.; Noble, M. Common-angle migration: A strategy for imaging complex media. *Geophysics* **2001**, *66*, 1877–1894. [CrossRef]
44. Sava, P.; Fomel, S. Angle-domain common-image gathers by wavefield continuation methods. *Geophysics* **2003**, *68*, 1065–1074. [CrossRef]
45. Wang, X.; Collett, T.S.; Lee, M.W.; Yang, S.; Guo, Y.; Wu, S. Geological controls on the occurrence of gas hydrate from core, downhole log, and seismic data in the Shenhu area, South China Sea. *Mar. Geol.* **2014**, *357*, 272–292. [CrossRef]
46. Su, M.; Sha, Z.B.; Qiao, S.H.; Yang, R.; Wu, N.Y.; Cong, X.R.; Liu, J. Sedimentary evolution since Quaternary in the Shenhu hydrate drilling area, northern South China Sea. *Chin. J. Geophys.* **2015**, *58*, 2975–2985. (In Chinese) [CrossRef]
47. Li, C.P.; You, J.C.; Zhu, W.J. Identification of bubble plumes and analysis of its correlation with resource environment. *Prog. Geophys.* **2016**, *31*, 2747–2755. (In Chinese) [CrossRef]
48. Chen, J.X.; Song, H.B.; Guan, Y.X.; Yang, S.X.; Bai, Y.; Geng, M.H. A preliminary study of submarine cold seeps applying seismic oceanography techniques. *Chin. J. Geophys.* **2017**, *60*, 604–616. (In Chinese) [CrossRef]
49. Zou, Z.; Zhang, L. Enhancing low-frequency water-column acoustic reflections in marine multichannel seismic data for seismic oceanography. *J. Acoust. Soc. Am.* **2021**, *150*, 3852–3860. [CrossRef] [PubMed]
50. Chen, C.Q.; Dai, H.T.; Gao, Q.; Chen, J.J.; Luo, W.L.; Wang, Z.R. A processing method for seismic data consistency under complex surface conditions and its applications. *Geophys. Geochem. Explor.* **2023**, *47*, 954–964. (In Chinese) [CrossRef]
51. Leroy, C.C. Development of simple equations for accurate and more realistic calculation of the speed of sound in seawater. *J. Acoust. Soc. Am.* **1969**, *46*, 216–226. [CrossRef]
52. Wang, F.; Mei, S.; Bu, X.; Yang, F.; Chen, J.; Zhao, Z. Quantifying the deep-sea cold seep gas flux using multibeam water column data: A case study in the Shenhu area of the South China Sea. *Deep-Sea Res. Part I Oceanogr. Res. Pap.* **2026**, *227*, 104644. [CrossRef]

Disclaimer/Publisher's Note: The statements, opinions and data contained in all publications are solely those of the individual author(s) and contributor(s) and not of MDPI and/or the editor(s). MDPI and/or the editor(s) disclaim responsibility for any injury to people or property resulting from any ideas, methods, instructions or products referred to in the content.